Hindawi
Geofluids
Volume 2023, Article ID 2401884, 16 pages
https://doi.org/10.1155/2023/2401884

Research Article

Pore-Scale Oil-Water Flow Behaviors in Different Development Adjustment Schemes for Enhancing Oil Recovery in Waterflooding

Jianjun Du,[1] Tao Xue,[1] Tao Ning,[1] Bingtao Hu,[2] Jinbiao Yu,[3] and Chen Wang[4]

[1]*The Management Headquarters of Water Injection Project, Yanchang Oil Field Co. Ltd., Yan'an 716000, China*
[2]*School of Human Settlements and Civil Engineering, Xi'an Jiaotong University, Xian, Shaanxi 710049, China*
[3]*Research Institute of Exploration and Development, Shengli Oilfield Company, Sinopec Group, Dongying 257015, China*
[4]*Key Laboratory of Auxiliary Chemistry and Technology for Chemical Industry, Ministry of Education, Shaanxi University of Science and Technology, Xi'an 710021, China*

Correspondence should be addressed to Chen Wang; wangchenhg@sust.edu.cn

Received 19 May 2022; Revised 23 December 2022; Accepted 8 May 2023; Published 14 June 2023

Academic Editor: Wei Sun

Development mode adjustment is an important measure to further enhance oil recovery after primary waterflooding. Investigating the oil-water flow behaviors in the pores is significant to deepening the understanding of the macrobehavior of waterflooding and the designation of the reservoir development plan. Previous studies mainly focused on the change in recovery factor and macroflow characteristics, while less attention was paid to the causes of the change in recovery factor and the difference in macrocharacteristics. In this paper, the numerical simulation technology by coupling the Navier-Stokes equation with the method of volume of fluid is employed to investigate the dynamic formation mechanism of the remaining oil at pore-scale in the primary waterflooding, and then the pore-scale oil-water two-phase behaviors under three waterflooding development adjustment schemes: changing flooding direction, turning extraction well to injection well, and increasing injection rate are studied. The research shows that when the viscous resistance of the water-bearing channel is less than the sum of the capillary barrier and drainage capillary resistance (the resistance in the displacement of wetting phase displacement using the nonwetting phase), the remaining oil is formed. Water➔oil➔water➔oil displacement mode is formed in the process of changing flow direction, which makes the force of the phase interface tend to balance, reduces the capillary effect in waterflooding, and improves oil recovery. In the process of developing the scheme of turning extraction into an injection well, through multipoint injection, it advances from the central water-bearing area to the oil-bearing area on both sides in multiple paths, forming a larger spatial spread range than that in the change of flooding direction. Under the influence of the capillary barrier effect and drainage capillary resistance, when the injection rate is increased, the remaining oil can restart to move only when the flowing rate exceeds a certain value. The small viscous resistance in the water-bearing channel and the lateral resistance from the capillary barrier limiting the lateral sweep of water are the primary reasons for the insignificant improvement of oil recovery under the condition of a low liquid injection rate. The findings of this study can help for better understanding of pore-scale flow mechanism behaviors and their influences on the macroscopic development features in the waterflooding process.

1. Introduction

Waterflooding is one of the most important measures to enhance oil recovery in oil field development. During waterflooding, crude oil migrates from water wells to oil wells under hydrodynamic conditions. Long-term waterflooding will increase the water cut of oil wells and reduce the waterflooding efficiency [1]. After waterflooding, about ~60% of the crude oil is still remained in the reservoirs [2]. After the initial waterflooding, the oil recovery can usually be further improved by adjusting the waterflooding scheme (such as by adjusting the injection and extraction direction,

turning extraction to the injection well, and increasing injection speed). During the implementation of the new adjustment scheme, the kinetic process of oil-water movement in these pores has changed, thereby promoting the displacement of the oil phase from the pores with the water phase. The development process of waterflooding is actually a comprehensive process of oil-water two-phase movement in a large number of pore channels. Deepening the research on the pore-scale flow behavior of oil-water two-phase in pore channels is of great significance for understanding the mechanism behind macroscopic phenomena and formulating field plans [3, 4].

The pore-scale oil-water two-phase flow in the reservoir is determined by both viscous force and capillary force. Previous researchers have systematically studied the influence of viscous and capillary effects on pore-scale two-phase flow. For example, when the fluid injection rate is high, viscous fingering is likely to form during waterflooding. Homsy systematically investigated viscous fingering in porous media and pointed out that viscous fingering is caused by the viscosity difference between the two phases [5]. The viscous fingering can cause the waterflooding front to intrude, thereby reducing the ultimate recovery rate. Effective suppression of viscous fingering is essential to enhance oil recovery. For instance, in the polymer flooding process, polymer with high viscosity are injected so as to decrease the oil-water viscosity ratio, increase the swept region of injection fluid [1, 6], and improve the recovery rate. When the injection rate is low, capillary fingering is more likely to be formed in waterflooding. Singh et al. summarized the fluid displacement process in the porous media in capillary-dominated flows [7]. It is found that when the capillary effect is too strong, the recovery rate is also low. Wettability can have a major impact on capillary effects. Hu et al. obtained a phase diagram of immiscible displacement in disordered porous media and investigated the effect of disorder feature and contact angle on the two-phase flow behaviors [8]. Yang et al. investigated the effect of the capillary effect on the remaining oil distribution in 3D porous media [9]. Lowering the capillary effect can improve the oil recovery rate. For instance, in the surfactant flooding process, residual oil starts to move by reducing the oil-water interfacial tension through adding surfactants to the displacement fluid [10]. For a given pore structure, the fluid behavior of the two phases depends on the relative magnitude of viscous action and capillarity. The capillary number is often used to characterize the relative magnitude of viscous and capillary effects. Adjusting the magnitude of the capillary number can alter the multiphase flow behavior during the waterflooding process. The immiscible two-phase flooding process in a two-dimensional porous structure was studied by Cottin et al., and the evolution process from capillary fingering to viscous fingering was obtained [11]. Tsuji et al. investigated the flooding process in a three-dimensional porous structure by varying the capillary numbers and viscosity ratios, getting the displacement diagram, and analyzing the macroscopic flow features in different displacement modes [12]. Guo et al. studied the effect of viscosity and interfacial tension on the distribution of residual oil distribution [13]. Besides viscous fingering and capillary fingering, influenced by the complexity of the pore structure, specific pore-scale flow behaviors, including the Haines jumps [14], the snap-off events [15–18], and the capillary barrier effect [1, 3, 19], have been investigated by many researchers but at an infancy stage.

Although extensive researches have been carried out on viscous and capillary effects on two-phase flow behavior, these works only focus on the phenomenological description and characterization of two-phase flow behavior in unidirectional displacement processes. There are few studies on the flow pore-scale characteristics of the two-phase flow behaviors and the effect of the spatial spread of water. After initial waterflooding, the oil-water spatial distribution is more complex than the initial oil-water distribution. Furthermore, less attention is paid to the dynamic mechanism of the flow process during the adjustment of the development mode.

The pore-scale direct numerical simulation technique is a powerful measure to investigate the pore-scale behaviors and their effects on the macroscopic flow characteristics [4, 20–22]. In this paper, the direct numerical simulation method based on the Navier-Stokes equation coupled with the volume of fluid method is used to simulate the oil-water movement process in a porous structure from a low-permeability sandstone numerically. The procedure for such a technique is given in Figure 1. Firstly, the sandstone is scanned using computed tomography (CT), and a CT image is obtained, as shown in Figure 1(a). After binary segmentation, a binary image is obtained, as shown in Figure 1(b). After vectorization of the binary image, a porous geometry is obtained, as shown in Figure 1(c). The geometry is initially filled with oil. Water is injected from port A and exits from port B. The final oil-water distribution is given in Figure 1(d). With the remaining oil after waterflooding as the initial water-oil distribution, three development adjustment processes of adjustment of the injection and extraction direction (inlet port C; outlet port D, Figure 1(e)), turning extraction to injection well (inlet ports A and B; outlet ports C and D, Figure 1(f)), and increasing injection rate (inlet port A; outlet port B, Figure 1(g)) are performed. Finally, the oil-water movement process and the pore-scale dynamic mechanism of oil-water flow behaviors are obtained through dynamic analysis. The work is arranged as follows: the numerical model for simulating oil-water two-phase flow is presented in Section 2, systematic analysis of the formation of residual oil at pore scale is followed, discussion of the flow behaviors in development adjustment schemes for enhancing oil recovery in waterflooding is followed, and conclusions are given in Section 4.

2. Pore-Scale Oil-Water Flow Dynamics

In this paper, the Navier-Stokes equation is used to describe the movement of oil and water, the volume of fluid (VOF) method is used to track the evolution of oil-water spatial distribution, and the wettability of the reservoir is described by the contact angle.

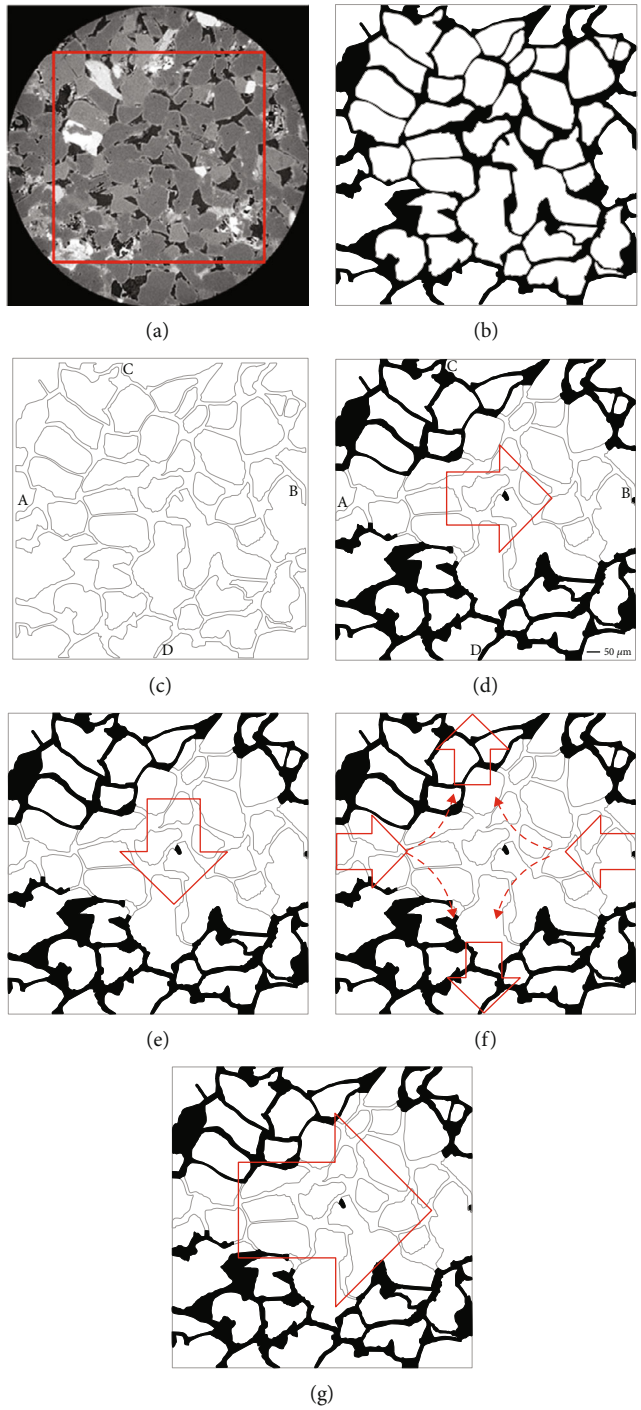

FIGURE 1: Procedure of the pore-scale direct numerical simulation technique for investigating flow behaviors in development adjustment in waterflooding. (a) Computed tomography image; (b) binary segmentation image; (c) porous geometry; (d) remaining oil distribution after waterflooding; (e) illustration of changing flooding direction; (f) illustration of turning extraction to an injection well; (g) illustration of increasing the flow rate.

2.1. Continuity Equation. The mass conservation of oil and water in the motion process can be described by the following equation:

$$\nabla \bullet \mathbf{u} = 0, \tag{1}$$

where $\mathbf{u}$ is the flowing velocity of water or oil. Oil and water are immiscible, and the velocity $\mathbf{u}$ at a certain position in space is the velocity of the fluid (oil or water) at that position.

2.2. Momentum Equation. The oil-water phase motion in the pore channels can be described by the Navier-Stokes equation

$$\frac{\partial \rho \mathbf{u}}{\partial t} + \nabla \bullet (\rho \mathbf{u}\mathbf{u}) - \nabla \bullet (\mu \boldsymbol{\tau}) = -\nabla p + \rho \mathbf{g} + \mathbf{F}_{\sigma}, \tag{2}$$

where ρ is the average density of water and oil; μ is the average viscosity; p is the pressure; $\mathbf{g}$ is gravity acceleration; and $\boldsymbol{\tau}$ is the deformation rate tensor of oil and water, as described by the following equation:

$$\boldsymbol{\tau} = \left(\nabla \mathbf{u} + (\nabla \mathbf{u})^{T}\right). \tag{3}$$

$\mathbf{F}_{\sigma}$ is the oil-water interface tension, given by

$$\mathbf{F}_{\sigma} = \sigma \delta_{s} k \mathbf{n}, \tag{4}$$

where σ is the oil-water interfacial tension coefficient, a physical parameter that remains constant in the simulation. δ_{s} is the oil-water interface area per unit volume, calculated by the following equation:

$$\delta_{s} = |\nabla \alpha|, \tag{5}$$

where α is the water volume fraction. $\mathbf{n}$ is the normal vector of the oil-water interface, which is calculated by the following equation:

$$\mathbf{n} = \frac{\nabla \alpha}{|\nabla \alpha|}. \tag{6}$$

k is the oil-water interface curvature, calculated by the following equation:

$$k = \nabla \bullet \mathbf{n}. \tag{7}$$

2.3. Equation of Water Volume Fraction. In this work, the volume fraction method is used to track the oil-water spatial distribution. The volume fraction of the water phase is denoted by α. When α is equal to 1, it means that the grid element is all occupied by water; when α is equal to 0, it means that the grid element is all occupied by the oil; and when α is between 0 and 1, the grid element includes the phase interface. The evolution of the water phase volume fraction is described by

$$\frac{\partial \alpha}{\partial t} + \nabla \bullet (\alpha \mathbf{u}) = 0. \tag{8}$$

2.4. Wettability. In order to consider the effect of wettability in the simulation, it is usually necessary to change the normal direction of the oil-water interface in the grid near the wall to the following form:

$$\mathbf{n} = \mathbf{n}_{w} \cos \theta + \mathbf{s}_{w} \sin \theta. \tag{9}$$

where θ is the contact angle; $\mathbf{n}_{w}$ is the face normal of the wall; $\mathbf{s}_{w}$ is the tangent vector of the interface perpendicular to the contact line.

2.5. Average Properties of Fluid. The density ρ and viscosity μ in equation (2) are the average density and viscosity of oil and water, which are calculated by the following two equations, respectively,

$$\rho = \alpha \rho_{w} + (1 - \alpha) \rho_{o}, \tag{10}$$

$$\mu = \alpha \mu_{w} + (1 - \alpha) \mu_{o}, \tag{11}$$

where ρ_{w} is the density of the water phase; ρ_{o} is the density of the oil phase; μ_{w} is the dynamic viscosity coefficient of the water phase; and μ_{o} is the dynamic viscosity coefficient of the oil phase.

Equations (1)–(11) constitute the basic equations of waterflooding. In this paper, these equations are discretized under the framework of finite volume, and the decoupling of velocity and pressure is realized by the PISO algorithm [23]. The convection term is discretized by the gamma format [24], and the oil-water interfacial tension is processed by the ghost-cell method [25].

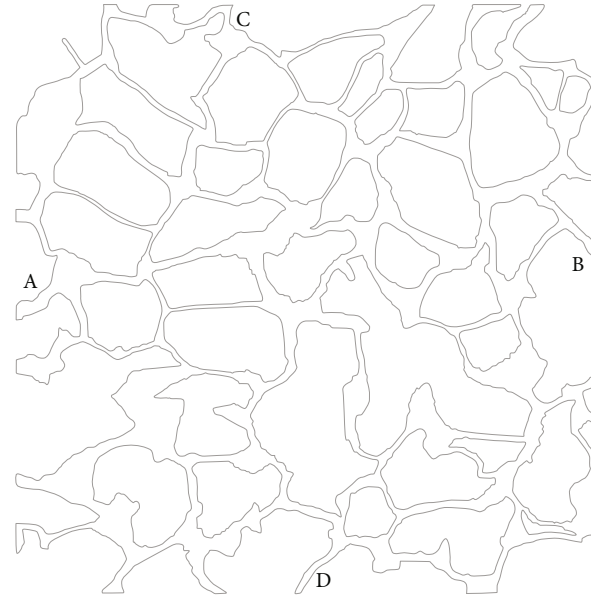

Figure 2: Digital core model.

Table 1: Boundary conditions.

	Field	Boundary conditions
Inlet	$\mathbf{u}$ (m/s)	Dirichlet
	p (Pa)	Neumann
	α	Dirichlet
Outlet	$\mathbf{u}$ (m/s)	Neumann
	p (Pa)	Dirichlet
	α	Neumann
Wall	$\mathbf{u}$ (m/s)	No slip
	p (Pa)	Neumann
	α	Contant angle

Table 2: Physical properties.

Phase	Physical parameters	Value
Oil	Dynamic viscosity μ (kg/(s·m))	5×10^{-3}
	Density ρ (kg/m^3)	800
Water	Dynamic viscosity μ (kg/(s·m))	10^{-3}
	Density ρ (kg/m^3)	1000
Oil-water interface	Interface tension coefficient σ (kg/s^2)	0.07

3. Discussions on Pore-Scale Flow Behaviors in Waterflooding

3.1. Physical Models and Numerical Settings. Figure 2 shows the digital core model used in the tests. The physical size of the core is 1.44 mm × 1.44 mm. The core is initially full of oil. During the simulation, water is injected into the pores from A to displace the oil in the core, and the liquid flows out from B. Other locations are closed. The boundary conditions used in the calculation process are shown in Table 1. The physical properties of the fluid are shown in Table 2.

3.2. Residual Oil Distribution after Waterflooding. The core shown in Figure 1 was initially filled with oil; port A is the injection port, and port B is the outflow port. Waterflooding was performed from port A to port B until no oil was produced. The residual oil distribution at this time is shown in Figure 3. The black in the picture is the remaining oil, and the rest is full of water. a, e, and f are the locations in the channel filled with water. b, c, and d are the locations of the oil-water interface at the throat-pore interface. It can be seen from the figure that the final remaining oil is distributed in the upper left corner, upper right corner, and lower part of the core area. b, c, and d in the figure are the positions where the oil-water interface stays. Along the channels a→e→f, the water is in motion. Therefore, there is a viscous pressure drop from a to e and from e to f. However, the fluids in channels a→b→g→e and a→b→g→d→f do not move, so there is no viscous pressure drop. Therefore, the pressure drop caused in the channel a→b→g→e is mainly balanced by the capillary pressure at the interfaces b and c.

When the oil-water interface approaches the pore-throat junction, it can change its direction and form a resistance [1], as shown in Figure 4. The interface morphology changes during the approaching process can be shown in Figure 4, and the capillary force changes are given in Figure 4(b) [1].

As shown in Figure 5, when $\theta + \beta > \pi/2$, the concave orientation of the interface is reversed during the movement. In the case of water wetness, the capillary force exhibits resistance, and there is a negative maximum value $p_c^{\min}$. When the power of the fluid is not enough to overcome the maximum resistance, the interface will stop moving, and the increasing and decreasing momentum in the process will only cause the interface to deform. This maximum resistance is given by

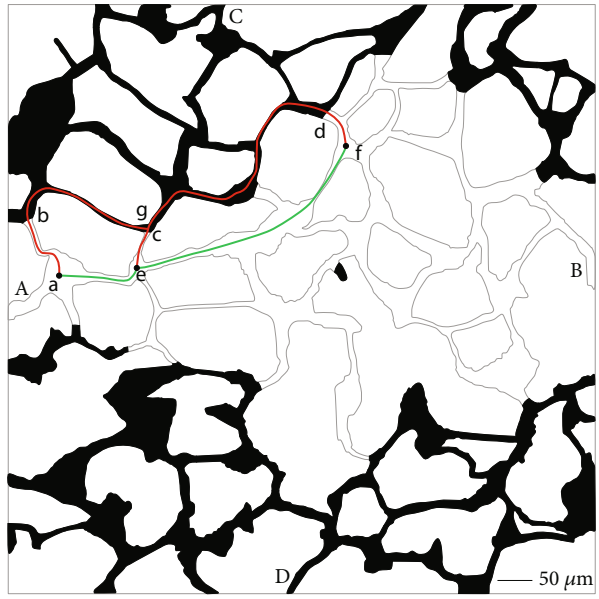

Figure 3: The residual oil distribution after waterflooding.

$$p_c^{\min} = \frac{\sigma \cos\left(\min\left(\theta + \beta, \pi\right)\right)}{R}. \tag{12}$$

This flow behavior is named as capillary barrier.

Position c and position d in Figure 5 are also at the pore-throat interface, from the pore to the throat. During the interfaces c and d that enter the throat from the pore, the mechanical state of the capillary will also change with the change of the channel radius, which can be divided into two types.

Case 1. When $\theta_o - \beta < 90^o$, in this case, the oil-water distribution before and after the oil-water interface enters the throat, as shown in Figure 6(a) (the oil-water interface is in the pore) and Figure 6(b) (the oil-water interface is in the throat);θ_o is the oil contact angle ($\theta o = 180\text{-}\theta$), and β is the opening angle of the channel. The capillary force is directed towards the throat, showing a positive dynamic state. After the oil-water interface enters the throat, the oil-water interface becomes the concave side of the water, and the capillary force is opposite to the moving direction, showing a resistance state.

In the process of entering the throat from the pore, the oil-water interface shape and capillary force will change at

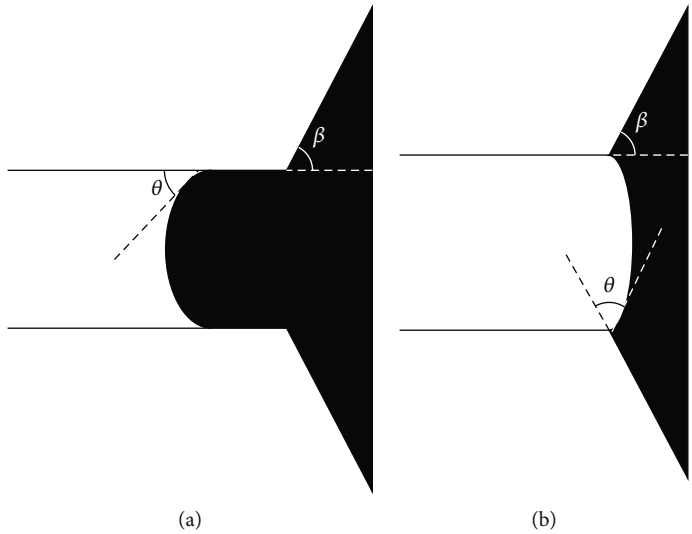

Figure 4: Oil-water distribution at different locations [1]. (a) The case where the oil-water interface is at the throat. (b) The case where the oil-water interface is at the junction of pore-throat; white: water; black: oil.

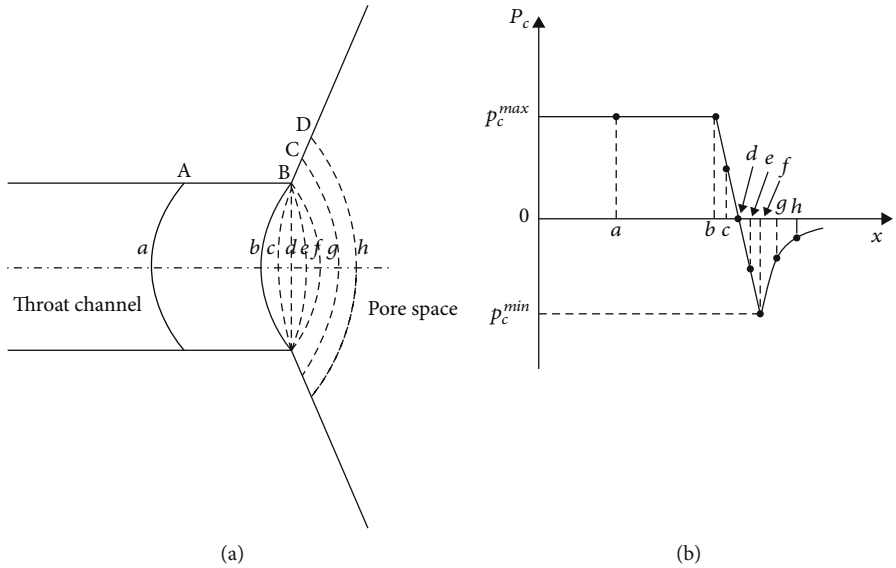

Figure 5: Sketch of oil-water interface shape and capillary force at different locations along the axis: (a) phase interface; (b) capillary force [1].

different positions, as shown in Figure 7(a) (changes of the oil-water interface and Figure 7(b) changes of the capillary force). When the oil-water interface approaches from the pore to the throat, the curvature radius of the oil-water interface gradually decreases. For example, from position A➔B, the corresponding capillary force gradually increases. When the three-phase contact line moves to the oil-water position *C*, the capillary force takes the maximum value

$$p_c^{\max} = \frac{\sigma \cos(\theta_o - \beta)}{r}, \tag{13}$$

where r is the throat radius. After the oil-water interface moves to position C, the three-phase contact line remains stationary, but the shape of the oil-water interface changes continuously, and the liquid level gradually evolves from concave to the right to concave to the left. At this time, the interfacial tension caused by the oil-water interface gradually changes from power to resistance. When a static contact angle is formed between the oil-water interface and the throat, the two-phase interfacial tension reaches the maximum resistance

$$p_c^{\min} = \frac{\sigma \cos(\theta_o)}{r}. \tag{14}$$

In all, the oil-water interface changes from the dynamic

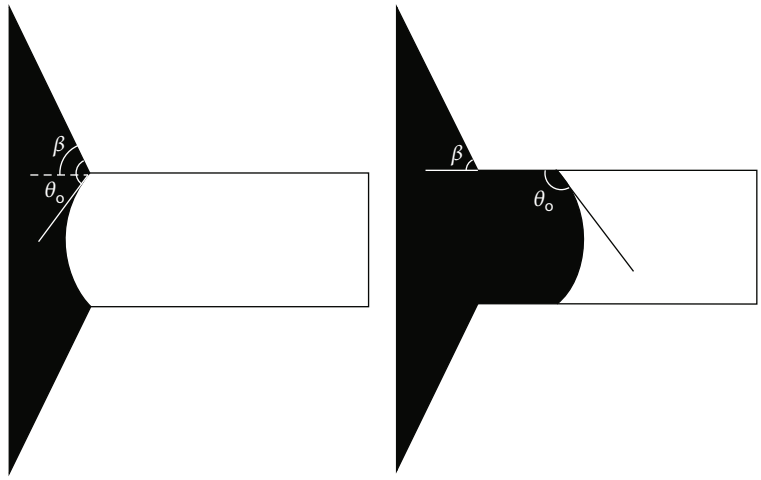

Figure 6: Oil-water distribution before and after the oil-water interface entering the throat in Case 1. (a) Oil-water interface in pores; (b) oil-water interface in the throat; white: water; black: oil.

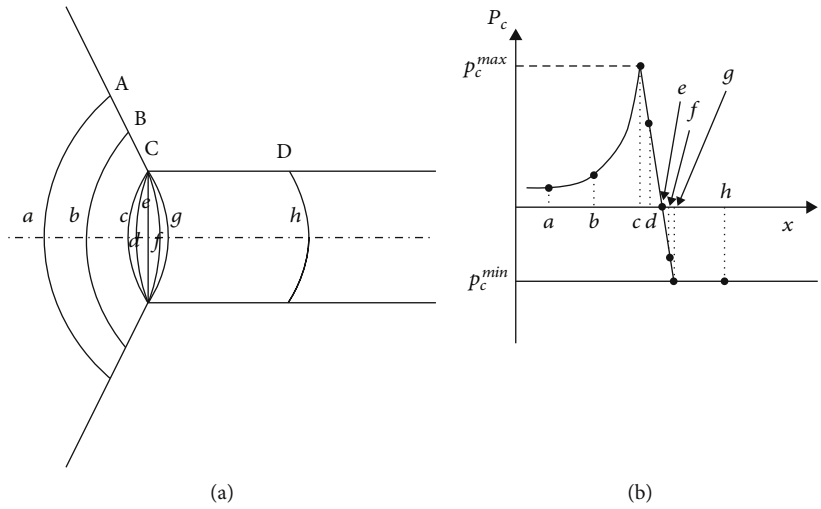

Figure 7: Oil-water shape along with capillary force before and after the oil-water interface entering the throat in Case 1. (a) Changes of oil-water interface shape; (b) changes of the capillary force.

state to the resistance state during the process of entering the throat from the pores.

Case 2. When $\theta_o - \beta > 90^o$, the oil-water interface before and after entering the throat from the pore as shown in Figure 8. (a) Oil-water interface in the pore; (b) oil-water interface in the throat. From this figure, it can be seen that the oil-water interface is concave to the oil side, whether in the pores or the throat, showing a resistance state.

Figure 9 shows the interface shape and the capillary force of the oil-water interface at different positions during the process of the oil-water interface entering the throat from the pores in Case 2. In the process of entering the throat from the pores, the curvature radius of the oil-water interface gradually decreases, and the size of the capillary force gradually increases (Figure 9(b)). The capillary force is negative, showing a resistance state. When the contact line arrived at position C, the oil-water interface only deforms, but the contact line remains stationary. When the oil-water interface and the throat exhibit a contact angle θ, the three-phase contact line moves along the direction C to D. At this time, the capillary force caused by the oil-water interface reaches a negative maximum value, and its magnitude can still be expressed by equation (14).

It can be seen from the above that whether restarting oil along the channel a→b→g→e or a→b→g→d→f as shown in Figure 2, the capillary force at interfaces b and c (or d) hinders the movement of oil and water. When the viscous pressure drop between a and e (or a and f) is higher than the maximum resistance threshold of capillary resistance at the interface of a and e (f), the waterflooding cannot restart the oil in the channel, and the oil therein is left.

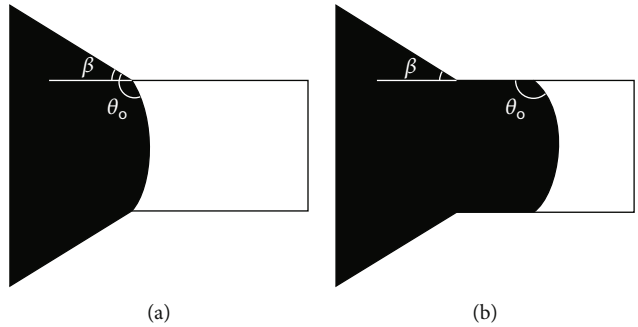

Figure 8: Oil-water distribution before and after the oil-water interface entering the throat in Case 2. (a) Oil-water interface in pores; (b) oil-water interface in the throat; white: water; black: oil.

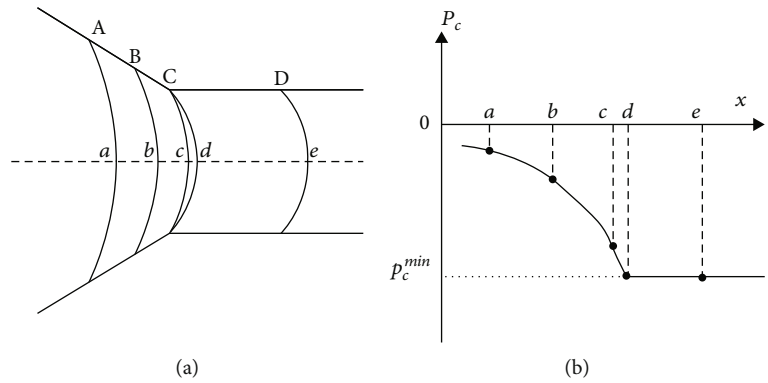

Figure 9: Oil-water shape along with capillary force before and after the oil-water interface entering the throat in Case 2. (a) Oil-water interface shape at different positions; (b) capillary force at different positions.

The capillary force caused by the displacement of the nonwetting phase using the wetting phase is named drainage capillary resistance in this work. The maximum drainage capillary resistance is named as drainage capillary threshold.

3.3. Flow Behaviors after Adjustment of the Flowing Direction. The remaining oil after waterflooding, as shown in Figure 3, is used as the initial state. The ports A and B are closed, and water is injected from port C and exits from port D, so as to simulate flow behaviors after adjusting the flowing direction. The fluid injection rate and fluid properties remain unchanged.

Figure 10 shows the oil-water distribution at different time points after changing flowing direction (a) 0.1 s; (b) 0.2 s; (c) 0.3 s; (d) 0.4 s; (e) final. It can be seen from the oil-water distribution in Figure 10(a) that after injection from the inlet C (see Figure 3), the oil-water interfaces reach points a, b, and c at 0.1 s, and oil-water interfaces o and n remain stationary, and the interface i migrates downward. The reason why the interfaces o and n remain stationary is that the interfaces are at the junction of the throat and the pore, and the nonwetting phase (oil) tries to enter the throat from the pores, showing a resistance state. The throat radius at o or n is smaller than the throat radius at i, making the resistance from the oil interface at o or n bigger than at i. Therefore, during the displacement process, it is easier for the fluid to migrate down by the i position into the next pore, form new interfaces at positions j, k, l, and m, and try to enter the throat through these interfaces. In the process of the nonwetting phase (oil) moving from the pores into the throat, the capillary force presents a state of resistance to the oil-water motion. The flooding direction is from top to bottom. During the downward migration of the oil-water interface, the lateral movement is small and the longitudinal movement is large. The position p is at the throat-pore junction, showing a capillary barrier effect that hinders fluid migration. Finally, the fluid migrates along channel 1, as shown in Figure 10(a), and the original capillary barrier at d breaks through, allowing the fluid to migrate downward, forming new interfaces such as e, f, and h. As the displacement progresses, the oil-water interface at position k continues to advance downward and enters the next pore. At 0.2 s, new interfaces are formed at positions k_1, k_2, k_3, and k_4 (as shown in Figure 10(b)). Channels passing positions k_1 and k_2 are perpendicular to the flow direction, and meanwhile, the oil interfaces show resistance to oil-water movement. As a result, these two channels are blocked. Once the channel passing k_1 is blocked, the original channel 1 shown in Figure 9(a) is blocked, and the pressure propagates along the new path, channel 2, prompting the formation of this path (as shown in Figure 10(b)). During the processes of the oil-water interface at k moving downwards, the

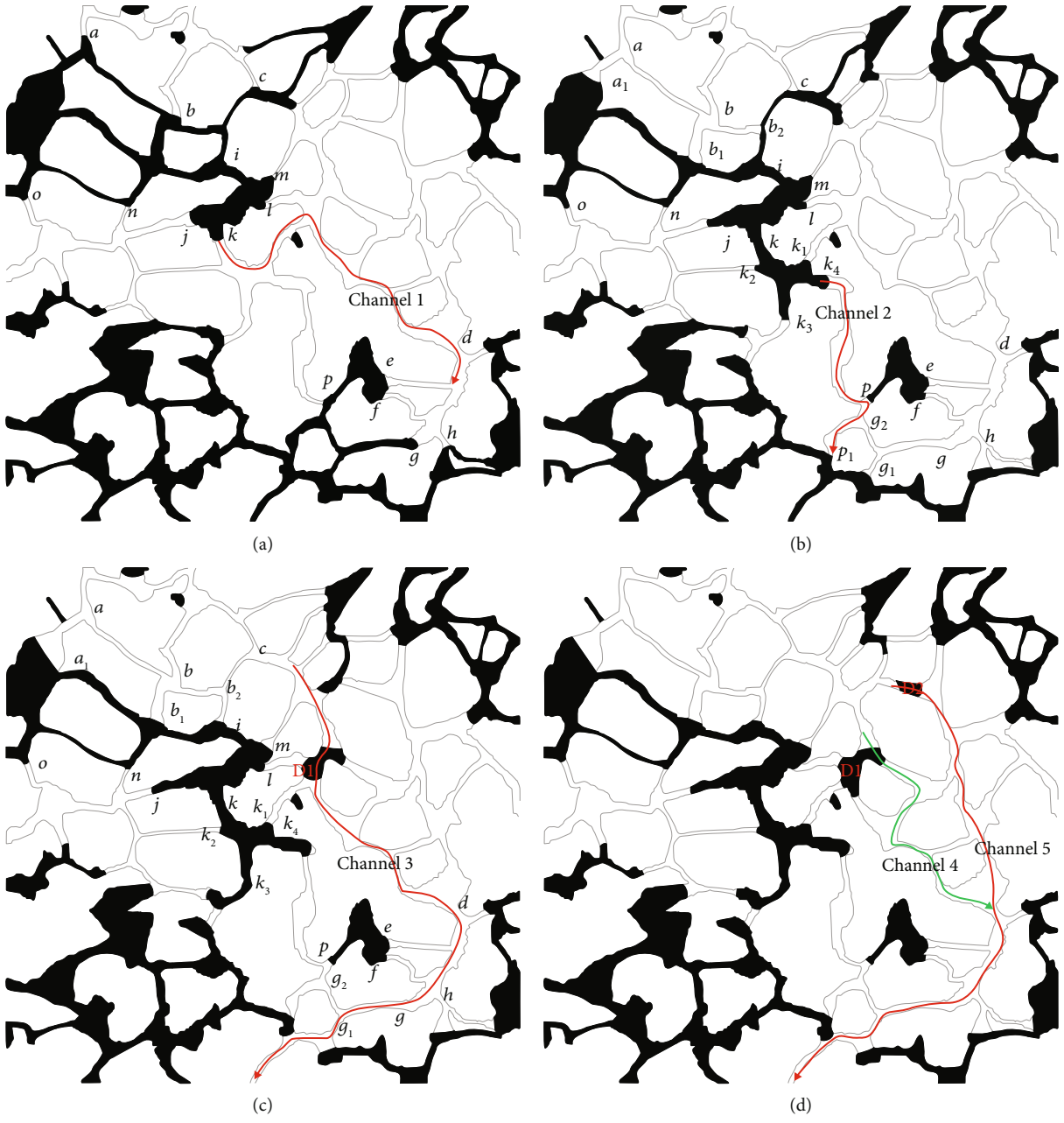

Figure 10: Continued.

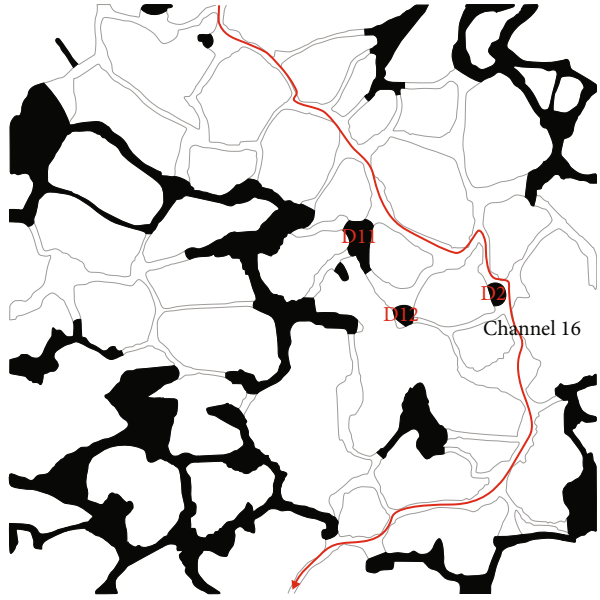

(e)

Figure 10: Oil-water distribution at different time points after adjustment of the flowing direction. (a) 0.1 s; (b) 0.2 s; (c) 0.3 s; (d) 0.4 s; (e) final.

interface at *g* moves downward, forming new interfaces at the positions of g_1 and g_2. At the same time, the capillary barrier at position breaks through, the oil-water interface moves downwards and meets the interface at g_2, and then moves downwards further until forming a new capillary barrier near p_1. As a result, the oil-water interface stops. Then, the capillary barrier at c and g_1 breaks through, forming channel 3, as shown in Figure 10(c). Subsequently, the oil-water interface at position c migrates downward and enters the next pore to form an oil block D1, as shown in Figure 10(c). As the fluid moves downward, the oil block D1 flows from the pores into the throat, which belongs to drainage capillary resistance. In this case, the oil-water interface presents a resistance to the oil-water movement. As a result, the upper half of channel 3 is blocked, and channels 4 and 5 (as shown in Figure 10(d)) form. Next, D1 is broken into D11 and D12, and D12 moves down along channel 4. When the D12 reaches the next pore, it blocks channel 4 for the resistance from the oil-water interface. At the same time, D2 migrates downward along channel 5, becomes oil droplets attached to the pore wall, and channel 6 forms. Finally, all the residual oil is blocked by the oil-water interface, and no oil is in motion, as shown in Figure 10(e).

From the above flow process, it can be found that affected by the capillary barrier and drainage capillary resistance, the oil-water flow path is constantly changing. Due to the lower resistance in the water-bearing area, the fluid tends to move in the high water-bearing area. After adjusting the flow direction, a displacement pattern of water→oil→water→oil is formed from the injection port to the outflow port. In this mode, the interfacial tension between water and oil tends to be more balanced, so that the macroscopic manifestation of the capillary effect is reduced.

3.4. Flowing Behaviors after Turning Extraction Well to Injection Well. The remaining oil after the initial waterflooding is used as the initial oil-water distribution; the A and B ports are used as the injection ports; and the C and D ports are used as the outlets for waterflooding. The water flow rates at port A and port B are the same, and the total water flow rate at port A and port B is the same as the total flow rate at port C in the case of Section 3.4. During the whole adjustment process, the properties of the fluid do not change.

Figure 11 shows the oil-water distribution at different times in this test: (a) 0.2 s, (b) 0.4 s, (c) 0.6 s, (d) 0.8 s, and (e) final. Comparing Figures 2 and 10(a), it can be found that after turning the extraction well into an injection well, three paths, channel 1, channel 2, and channel 3, were formed; two channels, channel 31 and channel 32, were formed downstream of channel 3, and channel 21 and channel 22 were formed at the downstream of the channel 2. As the displacement advances, at 0.4 s, two new interfaces at c_1 and c_2 are formed at the downstream of the interface c. These two interfaces are at the junction of the pore throat. The capillary barriers form at the junctions, hindering the further advancement of the fluid. At the same time, interface b migrates forward, and the interfaces at b_1 and b_2 are formed near the outlet. Under water-wet conditions, these two interfaces will hinder the movement of oil and water to the outlet due to drainage capillary resistance. The capillary pressure barrier and drainage capillary resistance at the junction of pore-throat cause the flow in channel 2 to stop, resulting in oil remaining. It can be seen from Figure 10(a) that in the early stage of displacement, the pressure from the left inlet is mainly conducted to the upper outlet. Once the upper flow path is blocked by capillary resistance, the capillary barrier formed at d will be broken through, resulting in

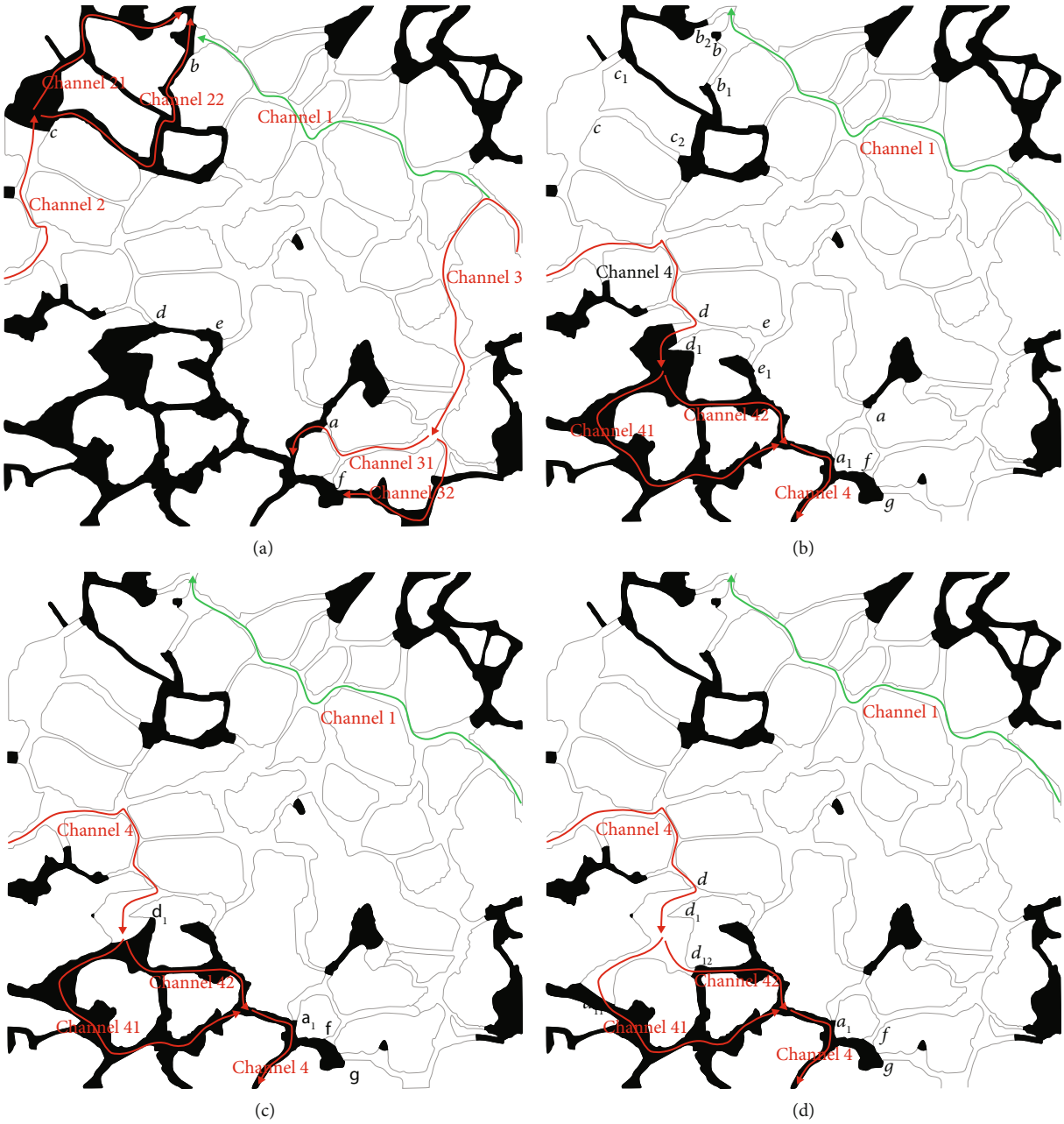

Figure 11: Continued.

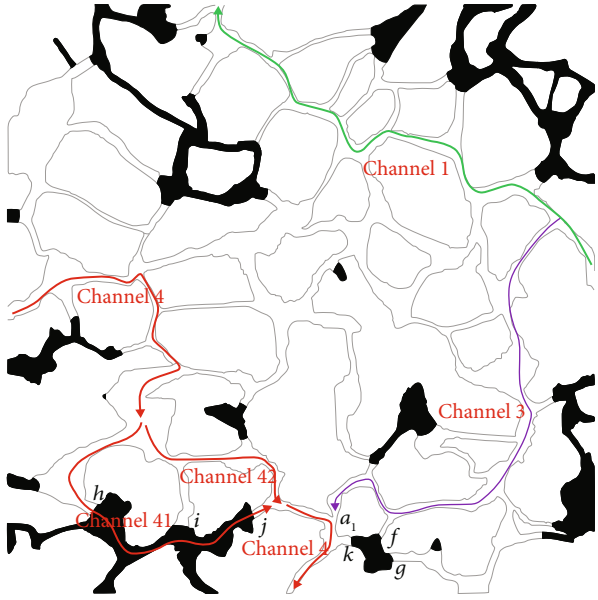

(e)

Figure 11: The oil-water distribution at different time points after turning extraction well to injection well. (a) 0.2 s; (b) 0.4 s; (c) 0.6 s; (d) 0.8 s; (e) final.

the formation of channel 4. Two branches, channel 41 and channel 42, in the middle of channel 4, are formed, as shown in Figure 11(b). As the displacement progresses, the branch channels channel 31 and channel 32 downstream of channel 3 are blocked by capillary barriers at a_1 and g, respectively, and channel 3 disappears. The oil-water interface in channel 4 on the left continuously migrates downwards, reaches d_1 at 0.6 s, and forms two interfaces, d_{11} and d_{12}, at 0.8 s. As the oil-water interface moves forward, new oil-water interfaces are formed at positions h, i, and j, as shown in Figure 11(e). The oil-water interfaces at positions h or i are the intersections of the pore throat, forming a capillary barrier and hindering the forward movement of the oil and water. The interface at position j also stops due to drainage capillary resistance. Under the action of the capillary barrier at position h and drainage capillary resistance at j, the oil-water movement in channel 41 stops. The oil-water interface in channel 42 migrates downward and contacts with the oil-water interface at a_1, causing the oil-water interface at this position to migrate downward, and fluid in channel 3 restarts. As the oil-water interface moves downward to the next pore, an oil-water interface k is formed, increasing the difficulty of the movement of the oil among the interfaces k, f, and g.

Compared with the case of the adjustment of the injection and extraction direction, in this case, the more complex the flow structure, the more flow paths are formed. The spatial sweep is larger than that in the case of adjustment of the injection and extraction direction, and the ultimate recovery rate is higher. On the premise of the same amount of injected liquid, the multipoint dispersed injection has a larger spatial sweep coefficient and a higher recovery rate than the single-point strong injection.

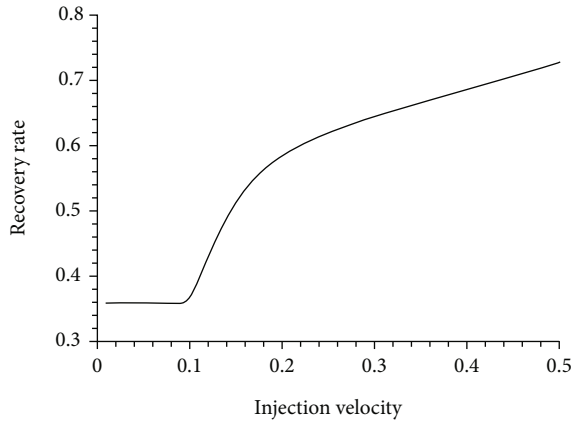

Figure 12: Changes of final recovery rate with increasing injection rate after initial waterflooding.

3.5. Flowing Behaviors after Increasing the Injection Flow Rate. Taking the oil-water distribution after waterflooding as the initial distribution, water was injected from port A at injection rates of 0.02 m/s, 0.05 m/s, 0.1 m/s, 0.2 m/s, and 0.5 m/s, respectively. After increasing the injection rate, the position of the inlet and outlet and the fluid properties remain unchanged.

Figure 12 shows the relationship between the final recovery rates at different injection rates in the test. It can be seen from the figure that the recovery rate did not change when the injection rate was increased from 0.01 m/s to 0.02 m/s and 0.05 m/s. The final recovery factor does not change until the injection rate increases above a certain threshold. When the injection rate is below this threshold, the residual oil will

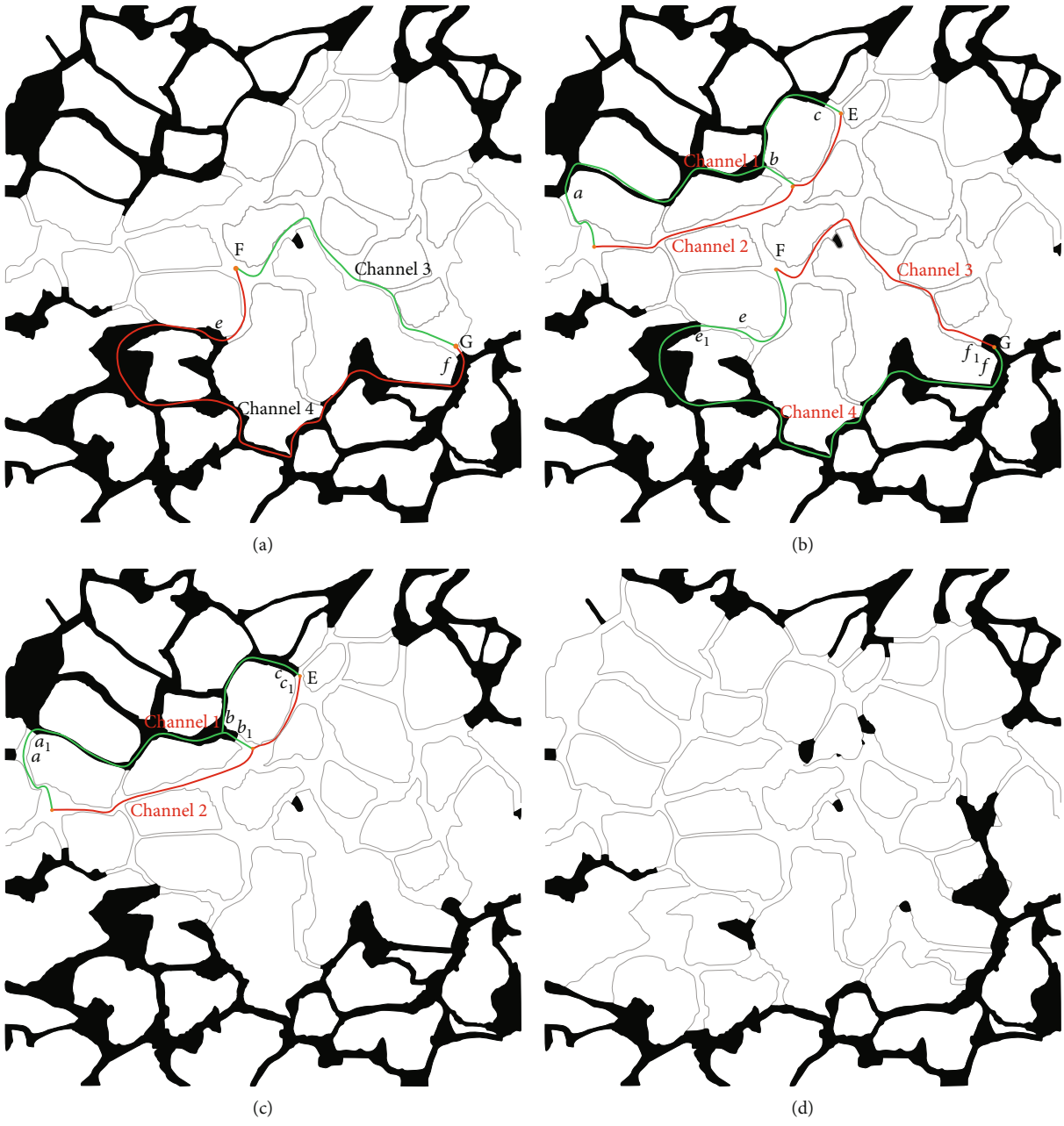

Figure 13: Continued.

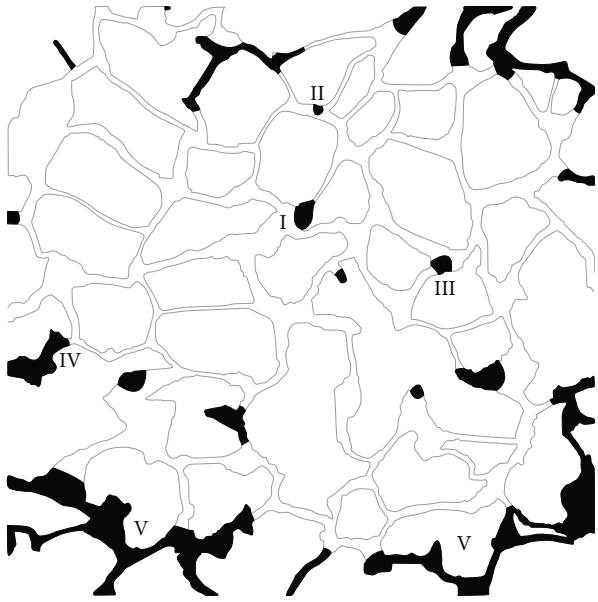

(e)

Figure 13: The final oil-water distribution under different injection rates after initial waterflooding. (a) 0.02 m/s; (b) 0.05 m/s; (c) 0.1 m/s; (d) 0.2 m/s; (e) 0.5 m/s.

not start to move. Once the injection rate is larger than this threshold, the recovery factor will increase significantly. With further increase in the injection rate further, the impact of the increased injection rate on the ultimate recovery rate becomes smaller.

Figure 13 shows the final oil-water distribution of waterflooding at different injection rates. It can be seen from the figure that in the case of low injection speed (such as 0.02 m/s as shown in Figure 13(a)) for waterflooding, the spatial distribution of remaining oil remains unchanged. When the injection speed is 0.05 m/s, the remaining oil in channel 4 moves. As shown in Figure 13(a), the water moves along channel 3 from point F to point G, so there is a pressure drop. However, along channel 4, from point F to point G, the fluid in this channel does not move. This is mainly due to the existence of interface e and interface f in channel 4, and the resultant force of the capillary forces of the two interfaces presents a resistance state. This resistance is balanced by the pressure drop from F to G. As the injection rate increases, the viscous pressure drop from F to G increases, and when this pressure drop exceeds the sum of the capillary forces of the two interfaces in channel 4, the oil in channel 4 moves. The oil-water interfaces at e and f move to positions e_1 and f_1, respectively. The sum of the capillary resistance formed by the two new interface positions balances the viscous pressure drop of the channel, and the oil-water movement stops. At low speed, the oil-water distribution in channel 1 is shown in Figure 13(b). In this state, the oil in channel 1 is trapped by the capillary force at the interfaces a, b, and c. When the viscous resistance of channel 2 exceeds the sum of the capillary resistance of the channel (for example, when the viscous resistance between CD exceeds the sum of the capillary forces of interfaces a and b, the remaining oil in the ab segment of channel 1 will move), the oil in the channel will start to move. When the injection speed is increased to 0.1 m/s, the oil in channel 1 moves. The oil-water interfaces a, b, and c move to a_1, b_1, and c_1, respectively. The oil-water movement stops when the capillary resistance of the oil-water interface at the new position balances the viscous pressure drop in channel 2. As the injection rate is further increased, a larger area of oil in the core begins to move, and it becomes more and more difficult for the remaining oil near the edge to move. When the injection speed is 0.2 m/s and 0.5 m/s, the power of waterflooding is greatly increased, resulting in the large-area movement of the remaining oil. The final remaining oil distribution is shown in Figures 13(d) and 13(e), respectively. With a larger injection flow rate, several different types of residual oil are formed, as shown in Figure 13(e). (I) droplet at the entrance of the pore-throat (I), the droplet at the pore walls (II), and the droplet at the outlet of the pore-throat (III), residual oil at the dead end of the pore-channels (IV), and the remaining oil in the unswept regions(V).

4. Summary and Conclusions

In this paper, direct numerical simulation technology based on the Navier-Stokes equation coupled with VOF is used to simulate the waterflooding process of a sandstone core. The kinetic formation mechanism of the remaining oil in the initial waterflooding was analyzed, and then the pore-scale oil-water flow behavior and pore-scale dynamics under three waterflooding development adjustment strategies: adjustment of the water flowing direction, turning the extraction well into an injection well, and increasing the injection rate were analyzed, and the following conclusions are drawn:

(1) The capillary barrier at the throat-pore junction and drainage capillary resistance caused by the oil-water interface is greater than the viscous resistance of the parallel water-bearing channels, which are the fundamental reasons for the formation of the remaining oil in the primary waterflooding

(2) In the process of adjusting the flow direction, the angle between the pressure gradient and the capillary force was changed. The macroscopic displacement mode of water→oil→water→oil is formed, which makes the capillary force at different interfaces in the same channel tend to balance. As a result, the effect of capillary force is reduced, and the oil recovery rate is improved. From a macroscopic point of view, newly injected water tends to move towards areas with a higher water fraction

(3) In the process of extraction into an injection well, multipoint injection is realized, so that the fluid advances from the central water-bearing zone to the oil-bearing zone on both sides in multiple paths, forming a larger spatial sweep region than that in the case of adjustment of the flowing direction, and the recovery rate is higher

(4) Affected by the capillary barrier and the drainage capillary resistance, in the mode of increasing the injection rate, the remaining oil can be used only when the injection rate reaches a certain threshold. The viscous resistance in the water-bearing channel is small, and the capillary barrier obstructs the lateral sweep of water laterally, which is the primary reason for the insignificant improvement of oil recovery rate under the condition of low extraction velocity

The pore-scale simulation method can reproduce the dynamic characteristics of two-phase fluid in pores and the influence of pore-scale flow behavior and mechanical characteristics on macroscopic flow characteristics. However, due to the limitation of computational load, the digital core used in this paper is rather small, and it is aimed at two-dimensional flow. The pore-scale flow in larger pore space in three-dimensional cases needs further study.

Alphabetic Letters

u: oil-water flowing velocity
t: time
p: pressure
g: gravity acceleration
$\mathbf{F}_\sigma$: oil-water interface tension
k: interface curvature
n: interface normal
r: pore channel radius.

Greek Letters

ρ: Oil-water average density
α: Water volume fraction
$\boldsymbol{\tau}$: The deformation rate tensor of oil and water
σ: Surface tension coefficient
δ_s: Interface area per unit volume
μ: Oil-water average viscosity
θ: Contact angle
β: Open angle.

Subscripts

wall: Wall
w: Water
o: Oil.

Superscripts

min: Minimum value
max: Maximum value.

Data Availability

The experimental data used to support the findings of this study are included within the manuscript and the supplementary materials.

Conflicts of Interest

The authors declared that there is no conflict of interest.

Authors' Contributions

C.Wang and J.Du proposed the main framework of the paper. J.Du, T.Xue, T.Ning, and B.Hu mainly wrote the paper. J.Du, J.Yu, and T.Xue analyze the data. All authors have read and agreed to the published version of the manuscript.

Acknowledgments

This research was funded by the National Natural Science Foundation of China, grant number: 22008148.

References

[1] T. Ning, M. Xi, B. Hu, L. Wang, C. Huang, and J. Su, "Effect of viscosity action and capillarity on pore-scale oil–water flowing behaviors in a low-permeability sandstone waterflood," *Energies*, vol. 14, no. 24, p. 8200, 2021.

[2] M. Zallaghi and A. R. Khazali, "Experimental and modeling study of enhanced oil recovery from carbonate reservoirs with smart water and surfactant injection," *Fuel*, vol. 304, article 121516, 2021.

[3] X. Liu, L. Wang, J. Wang, and J. Su, "Pore-scale simulation of particle flooding for enhancing oil recovery," *Energies*, vol. 14, no. 8, p. 2305, 2021.

[4] J. Su, G. Chai, L. Wang et al., "Direct numerical simulation of pore scale particle-water-oil transport in porous media," *Journal of Petroleum Science and Engineering*, vol. 180, pp. 159–175, 2019.

[5] G. M. Homsy, "Viscous fingering in porous media," *Annual Review of Fluid Mechanics*, vol. 19, no. 1, pp. 271–311, 1987.

[6] J. Verma and A. Mandal, "Potential effective criteria for selection of polymer in enhanced oil recovery," *Petroleum Science and Technology*, vol. 40, no. 7, pp. 879–892, 2022.

[7] K. Singh, M. Jung, M. Brinkmann, and R. Seemann, "Capillary-dominated fluid displacement in porous media," *Annual Review of Fluid Mechanics*, vol. 51, no. 1, pp. 429–449, 2019.

[8] R. Hu, T. Lan, G. J. Wei, and Y. F. Chen, "Phase diagram of quasi-static immiscible displacement in disordered porous media," *Journal of Mechanics*, vol. 875, pp. 448–475, 2019.

[9] Y. F. Yang, S. B. Cai, J. Yao et al., "Pore-scale simulation of remaining oil distribution in 3D porous media affected by wettability and capillarity based on volume of fluid method," *International Journal of Multiphase Flow*, vol. 143, article 103746, 2021.

[10] J. W. Su, L. Wang, Z. L. Gu, Y. Zhang, and C. Chen, "Advances in pore-scale simulation of oil reservoirs," *Energies*, vol. 11, no. 5, p. 1132, 2018.

[11] C. Cottin, H. Bodiguel, and A. Colin, "Drainage in two-dimensional porous media: from capillary fingering to viscous flow," *Physics*, vol. 82, no. 4, article 046315, 2010.

[12] T. Tsuji, F. Jiang, and K. T. Christensen, "Characterization of immiscible fluid displacement processes with various capillary numbers and viscosity ratios in 3D natural sandstone," *Advances in Water Resources*, vol. 95, pp. 3–15, 2016.

[13] Y. H. Guo, L. Zhang, G. P. Zhu et al., "A pore-scale investigation of residual oil distributions and enhanced oil recovery methods," *Energies*, vol. 12, no. 19, 2019.

[14] S. Berg, H. Ott, S. A. Klapp et al., "Real-time 3D imaging of Haines jumps in porous media flow," *Proceedings of the National Academy of Sciences of the United States of America*, vol. 110, no. 10, pp. 3755–3759, 2013.

[15] J. G. Roof, "Snap-off of oil droplets in water-wet pores," *Society of Petroleum Engineers Journal*, vol. 10, no. 1, pp. 85–90, 1970.

[16] Z. Li, Z. L. Gu, R. Li et al., "Investigation on droplet dynamic snap-off process in a short, abrupt constriction," *Chemical Engineering Science*, vol. 235, article 116496, 2021.

[17] L. M. Cha, C. Y. Xie, Q. H. Feng, and M. Balhoff, "Geometric criteria for the snap-off of a non-wetting droplet in pore-throat channels with rectangular cross-sections," *Water Resources Research*, vol. 57, no. 7, p. e2020WR029476, 2021.

[18] Z. Li, Z. Gu, R. Li et al., "A geometrical criterion for the dynamic snap-off event of a non-wetting droplet in a rectangular pore–throat microchannel," *Physics of Fluids*, vol. 34, no. 4, article 042014, 2022.

[19] H. S. Rabbani, B. Z. Zhao, R. Juanes, and N. Shokri, "Pore geometry control of apparent wetting in porous media," *Scientific Reports*, vol. 8, no. 1, pp. 1–8, 2018.

[20] G. L. Chai, L. Wang, Z. L. Gu et al., "A consistent sharp interface fictitious domain method for moving boundary problems with arbitrarily polyhedral mesh," *International Journal for Numerical Methods in Fluids*, vol. 93, no. 7, pp. 2065–2088, 2021.

[21] J. W. Su, G. L. Chai, L. Wang et al., "Direct numerical simulation of particle pore-scale transport through three- dimensional porous media with arbitrarily polyhedral mesh," *Powder Technology*, vol. 367, pp. 576–596, 2020.

[22] J. W. Su, G. L. Chai, L. Wang et al., "Pore-scale direct numerical simulation of particle transport in porous media," *Chemical Engineering Science*, vol. 199, pp. 613–627, 2019.

[23] R. I. Issa, "Solution of the implicitly discretised fluid flow equations by operator- splitting," *Journal of Computational Physics*, vol. 62, no. 1, pp. 40–65, 1986.

[24] H. Jasak, H. G. Weller, and A. D. Gosman, "High resolution NVD differencing scheme for arbitrarily unstructured meshes," *International Journal for Numerical Methods in Fluids*, vol. 31, no. 2, pp. 431–449, 1999.

[25] M. M. Francois, S. J. Cummins, E. D. Dendy, D. B. Kothe, J. M. Sicilian, and M. W. Williams, "A balanced-force algorithm for continuous and sharp interfacial surface tension models within a volume tracking framework," *Journal of Computational Physics*, vol. 213, no. 1, pp. 141–173, 2006.